

Observation of anomalous information scrambling in a Rydberg atom array

Xinhui Liang^{1,2,*}, Zongpei Yue^{1,3,*}, Yu-Xin Chao^{1,3}, Zhen-Xing Hua^{1,3}, Yige Lin⁴, Meng Khoon Tey^{1,3,5†} and Li You^{1,2,3,5‡}

¹State Key Laboratory of Low Dimensional Quantum Physics, Department of Physics, Tsinghua University, Beijing 100084, China

²Beijing Academy of Quantum Information Sciences, Beijing 100193, China

³Frontier Science Center for Quantum Information, Beijing, China

⁴Division of Time and Frequency Metrology, National Institute of Metrology, Beijing 100029, People's Republic of China

⁵Hefei National Laboratory, Hefei, Anhui 230088, China

* These authors contributed equally to this work.

† mengkhoon.tey@mail.tsinghua.edu.cn

‡ lyou@mail.tsinghua.edu.cn

Quantum information scrambling, which describes the propagation and effective loss of local information, is crucial for understanding the dynamics of quantum many-body systems¹⁻³. In general, a typical interacting system would thermalize under time evolution, leading to the emergence of ergodicity and linear lightcones of information scrambling⁴. Whereas, for a many-body localized system strong disorders give rise to an extensive number of conserved quantities that prevent the system from thermalization^{5,6}, resulting in full ergodicity breaking and a logarithmic lightcone for information spreading⁷⁻⁹. Here, we report the experimental observation of anomalous information scrambling in an atomic tweezer array. Working in the Rydberg blockade regime, where van der Waals interaction dominates, we observe a suppressed linear lightcone of information spreading characterized by out-of-time-order correlators for the initial Néel state, accompanied by persistent oscillations within the lightcone. Such an anomalous dynamics differs from both generic thermal and many-body localized scenarios. It originates from weak ergodicity breaking and is the characteristic feature for quantum many-body scars¹⁰. The high-quality single-atom manipulations and coherent constraint dynamics, augmented by the effective protocol for time-reversed evolution we demonstrate, establish a versatile hybrid analog-digital simulation approach to explore diverse exotic non-equilibrium dynamics with atomic tweezer arrays.

Quantum information scrambling in closed many-body systems has attracted significant attention as a method to explore the dynamics of far-from-equilibrium physics. Characterized by the dispersal of local information to entire system through many-body entanglements and correlations, this process is key to understanding the dynamics of thermalization and the evolution of quantum systems towards equilibrium. A powerful metric for quantifying the intricate scrambling of local information is out-of-time-order correlators (OTOCs)¹⁻³. Here we focus on the form of the squared commutator

$$C(t) = \langle \psi | [W(t), V]^\dagger [W(t), V] | \psi \rangle, \quad (1)$$

where $W(t) = e^{i\mathcal{H}t} W e^{-i\mathcal{H}t}$ represents the operator's evolution in the Heisenberg picture. These matrices constitute a measure of how fast the noncommutativity between two quantum operations is established.

The OTOCs have been studied in various physical systems, ranging from nuclear spins¹¹⁻¹³, trapped ions¹⁴⁻¹⁷, superconducting

circuits¹⁸⁻²¹, to NV centers²². A primary experimental challenge to measure OTOCs is the implementation of time-reversed many-body dynamics, which is in principle possible for unitary evolutions but inherently difficult to achieve in practice, mainly due to large system sizes, limited experimental control capability of the many-body interactions, and inevitable experimental noises. Previous studies adopted a variety of approaches to realize the time-reversed evolution, either using digital simulation with quantum gates and the Suzuki-Trotter decomposition^{11-13, 15, 17, 18, 23} or fully analog simulation with controllable interactions through additional Hamiltonian engineering^{14, 19-21}. Randomized measurements^{16, 24, 25} have also been used to circumvent time-reversed evolution.

Atomic tweezer arrays offer a promising platform with inherent single-qubit addressability and the potential to scale up to large sizes with programmable configurations in various dimensions²⁶⁻³². The strong van der Waals interactions, predominant in atomic tweezer array system, give rise to Rydberg blockade mechanism and rich quantum phases³³⁻³⁵. The presence of local dynamic constraints is also believed to give rise to quantum many-body scars^{33, 36-39}, a notable departure from the nominal understanding of ergodicity in eigenstate thermalization hypothesis (ETH)^{40, 41}. Quantum many-body scars are a special class of eigenstates embedded in a sea of thermal eigenstates that partially break ergodicity^{37, 38}. Different from the previously observed dynamics of OTOCs inside the emergent lightcone in chaotic systems, anomalous information scrambling behaviours is predicted in systems with quantum many-body scars¹⁰, yet have not been observed until this experiments.

This work reports the observation of anomalous information scrambling in a Rydberg atom array with ⁸⁷Rb atoms. By working in the Rydberg blockade regime where van der Waals interaction is the dominant energy scale, the system simplifies into the kinetically constrained PXP model³⁷ iff nearest neighbor interactions are taken into consideration. The challenge of reversing the interaction sign is bypassed in the truncated smaller Hilbert space of the PXP model, and we are able to successfully implement and measure the OTOCs in experiment and observe the emergent anomalous linear lightcone with persistent periodic oscillations inside. Our results show that OTOCs for the initial Z_2 Néel states exhibit smaller butterfly velocity at compared to the pro-typical one with all atoms in the ground state. Within the lightcone, anomalous spatial-temporal structures, specifically the honeycomb-like persistent oscillations, where OTOC peaks at the same time, are observed. Analogous features are also observed in the local Rydberg atom density and two-body correlation in time-forward dynamics. The observed linear lightcone with persistent periodic oscillations is distinct from both thermal and many-body localized systems, which exhibit either no oscillation inside the linear lightcone or a logarithmic lightcone. It signifies unusual breakdown of thermalization and persistent backflow of quantum information in quantum many-body scarred systems.

Experimental setup. Our experimental setup is illustrated in Fig. 1a. Neutral ⁸⁷Rb atoms are rearranged into a linear single atom array with equal spacing. They are initialized in the electronic ground state $|5S_{1/2}, F=2, m_F=2\rangle$ and coupled to the Ryd-

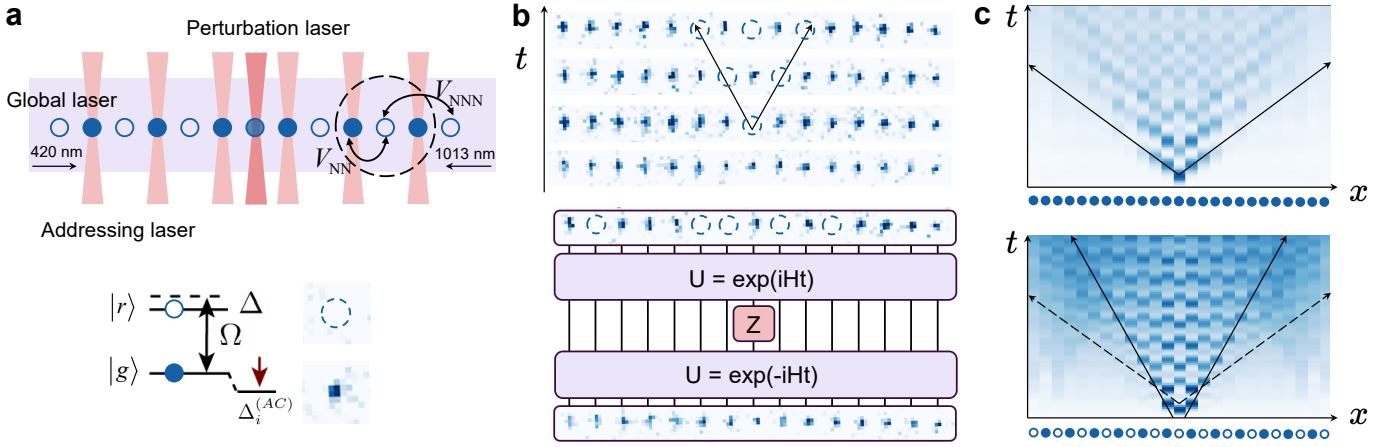


Figure 1 | Quantum information scrambling in a constrained Rydberg atom array. **a**, The experimental setup consists of a one-dimensional defect-free atom array. Qubits are encoded into atomic ground (solid circle) and Rydberg (empty circle) states. Its evolution is driven by counter-propagating global lasers with two-photon Rabi frequency Ω and detuning Δ , while additional programmable beams provide for single-qubit AC Stark shifts $\Delta_i^{(AC)}$ for addressable qubit rotations and select initial state preparation. The state readout is through destructive imaging, wherein the ground state is recaptured while the Rydberg state is irreversibly lost and subsequently depicted by a dashed empty circle. Nearest neighbour blockade $V_{NN} \gg \Omega \gg V_{NNN}$ constrains many-body dynamics to a subspace where two nearby atoms cannot be simultaneously in Rydberg states. **b**, The experimental sequence to measure the OTOCs. Local disturbance in the form of a single-qubit rotation Z is applied to the central atom of the chain between the time-forward and time-reversed evolutions. Information scrambling, characterized by the OTOC, is probed by counting the difference of local Rydberg atom density between the initial and final states at varying evolution time. **c**, Dynamics of quantum information scrambling numerically calculated for two different initial states. The generic initial states, such as $|g\rangle = |gg\dots g\rangle$, show a linear lightcone and the contrast of OTOCs inside the lightcone decays fast, while the Z_2 Néel states, like $|Z_2\rangle = |rgrg\dots rgr\rangle$, which possesses a large overlap with the scarred subspace, exhibits slower information spreading with persistent oscillations inside the lightcone.

berg state $|70S_{1/2}, J = 1/2, m_J = 1/2\rangle$ via the intermediate state $|6P_{3/2}, F = 3, m_F = 3\rangle$ using two counter-propagating global lasers at 420 nm and 1013 nm, respectively. The effective two-photon Rabi frequency is denoted by Ω and the bare two-photon detuning by Δ . When excited into the Rydberg state, neighbouring atoms interact via a strong, repulsive van der Waals interaction $V(\mathbf{r}_{ij})$, which decays by the sixth power of inter-atomic separation \mathbf{r}_{ij} . The many-body Hamiltonian ($\hbar = 1$) is approximately described by

$$H = \frac{\Omega}{2} \sum_i \sigma_x^{(i)} - \sum_i (\Delta - \Delta_i^{(AC)}) n_i^r + \sum_{i < j} V(\mathbf{r}_{ij}) n_i^r n_j^r, \quad (2)$$

where i indexes atomic sites in the array, $n_i^r = (1 + \sigma_z^{(i)})/2$ is the on site Rydberg atom density operator and $\Delta_i^{(AC)}$ represents the AC-stark shift by individual addressing lasers.

In the limit of perfect nearest-neighbor (NN) blockade and negligible interactions for next nearest neighbors (NNN) and beyond, $V_{NN} \gg \Omega \gg V_{NNN}$, the many-body dynamics are governed by the PXP model:

$$H = \frac{\Omega}{2} \sum_{i=1}^{L-1} P_{i-1} \sigma_x^{(i)} P_{i+1}, \quad (3)$$

where $P_i = (1 - \sigma_z^{(i)})/2$ is the ground state projection operator and two-photon detuning $\Delta - \Delta_i^{(AC)}$ is set to 0. This model imposes the constraint that an atom can be excited to Rydberg state or deexcited back to ground state if its nearest neighbors are not in Rydberg states. Although it remains non-integrable and its dynamics is chaotic, the PXP Hamiltonian uniquely possesses a small fraction of scarred eigenstates that violate ETH³⁸, manifested by periodic recurrences in the dynamics of entanglement entropy and local correlation function³⁷. The Z_2 Néel state $|Z_2\rangle = |rgrg\dots rgr\rangle$ is of particular interest since it can be directly prepared and has a large overlap with the scarred subspace, making it a simple yet pivotal model for exploring information scrambling in a constrained system.

Measuring OTOCs. The measurement of OTOC for arbitrary initial states is challenging. We simplify the task by taking specific representative product states as initial states, as detailed in the Supplementary Information (SM) Sec. II⁴². The selected OTOCs are measured through Loschmidt echo procedures as shown in Fig. 1b, where a precisely prepared initial state first undergoes time-forward evolution and then time-reversed evolution, intended to restore the system to its initial configuration. In between the time-forward and time-reversed evolution, a local operator σ_z is applied to the central or the 7th atom of the 13 atom chain employed, disrupting the full reversibility. The choice of a local disturbance $W = \sigma_z^{(7)}$ and measurement $V = \sigma_z^{(i)}$ provides the spatial resolution of information scrambling. The OTOC thus simplifies to $C_i(t) = \langle \psi | [\sigma_z^{(7)}(t), \sigma_z^{(i)}]^\dagger [\sigma_z^{(7)}(t), \sigma_z^{(i)}] | \psi \rangle / 4 = |\langle n_i^r(t) \rangle - \langle n_i^r(0) \rangle|$, where $\langle n_i^r(t) \rangle$ represents the probability that i th atom stays in the Rydberg state after completing Loschmidt echo with total evolution time of $2t$. A nonzero valued $C_i(t)$ indicates the existence of finite information transport from the middle of the array to other sites. Dividing by 4 gives the convenient normalization as the OTOC value now reduces to counting the density of Rydberg atoms after Loschmidt echo. By adjusting the duration of Loschmidt echo and the site index of measurement operator, we obtain time- and site-resolved OTOCs.

Time-reversed evolution The time-reversed evolution as required poses a significant challenge for many analog simulators. Fortunately for our system, we need only to imprint a global π phase jump to the Rydberg coupling laser (see Methods Sec. I), which introduces a negative sign to Ω and consequently to the overall PXP Hamiltonian, and facilitates time-reversed evolution. To verify the efficacy of this solution, we measure the Loschmidt echo with two representative initial states, the $|g\rangle = |gg\dots g\rangle$ and $|Z_2\rangle$ states. The results are shown in Fig. 2. The averaged Rydberg atom occupation is found to be approximately symmetric with respect to the phase-jumping point, proving that the effective Hamiltonian before and after the jump are approximately opposite in sign.

The infidelity of the time-reversed evolution arises primarily from the next-nearest-neighbor interactions, which are neglected in the PXP

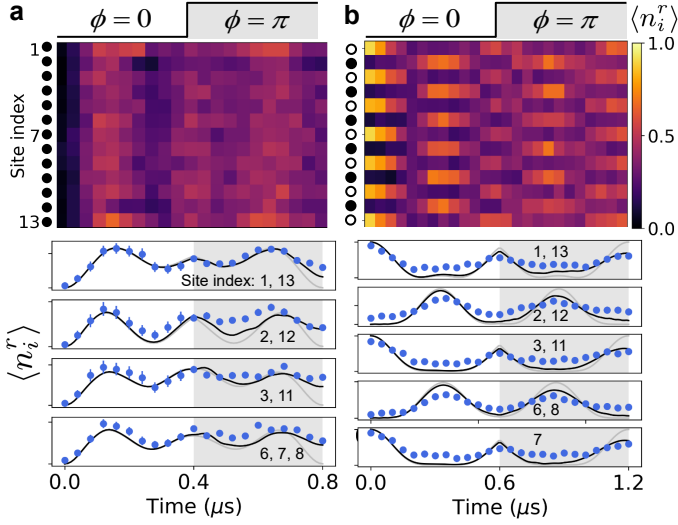


Figure 2 | Time-reversed evolution for different initial states. Time-reversed evolution is implemented through a π phase jump of the global Rydberg laser, which changes the sign of the Rabi frequency in the effectively equivalent PXP model. The evolution starts from the state $|g\rangle = |gg\dots g\rangle$ in **a** and the $|Z_2\rangle = |rgrg\dots rgr\rangle$ Néel state in **b**. The white and gray backgrounds in the headers indicate the phases before and after the phase jump, respectively. The upper panel displays the averaged Rydberg atom density at each site, while the lower panel provides for a detailed comparison of the experimental results (symbols) with numerical simulations based on the complete model Hamiltonian Eq. (2) (black lines) and PXP Hamiltonian Eq. (3) (grey lines). The deviations between the experimental data and the perfect time-reversed evolution of the PXP model primarily stem from the finite next-nearest-neighbor interactions in the actual model Hamiltonian. The contrast in the $|Z_2\rangle$ Néel state evolution is reduced due to imperfect preparation of the initial state.

model. To mitigate this infidelity and achieve a more accurate time-reversed evolution, we have included an extra detuning at approximately twice the next-nearest-neighbor interaction strength V_{NNN} (see SM Sec. IV⁴²).

Emergent lightcone with initial state $|g\rangle$. The experimental and numerical results for the OTOC are presented in Fig. 3a for the initial state $|g\rangle$. A linear lightcone-like pattern of operator spreading is clearly visible, with the fitted butterfly velocity at about 10 sites per microsecond, which aligns well with numerical simulations and effectively represents the speed of information scrambling for a typical state.

Comparing the measured OTOC results to numerical ones, the observed contrast is found lower than expected. Such degradation can be attributed primarily to decoherence that arise from three sources: variations in the atomic positions within the chain, which cause phase imprinting errors; the consequent fluctuations in the van der Waals interactions between atoms; and single-atom decoherence. Our experimental data compares well to numerical calculations shown in blue dashed lines after considering these decoherence effects. This agreement implicates that the dominant impact of decoherence is on the contrast of OTOC. The fundamental dynamics of quantum information scrambling, as characterized by the butterfly velocity, remains largely unaffected by the decoherence sources present in our system.

Anomalous information scrambling with initial Néel state. For the second set of experiments with $|Z_2\rangle$, the Z_2 Néel state is prepared by adiabatically driving the atoms $|g\rangle$ to $|r\rangle$ globally, while inhibiting such excitations for the odd sites by employing additional addressing lasers as shown in Fig. 1 (Methods Sec. I). The measurement results are presented in Fig. 3. Besides a slower butterfly velocity, we observe oscillatory operator spreading within the lightcone, in stark contrast to the behavior observed for the state $|g\rangle$. While slower operator spread-

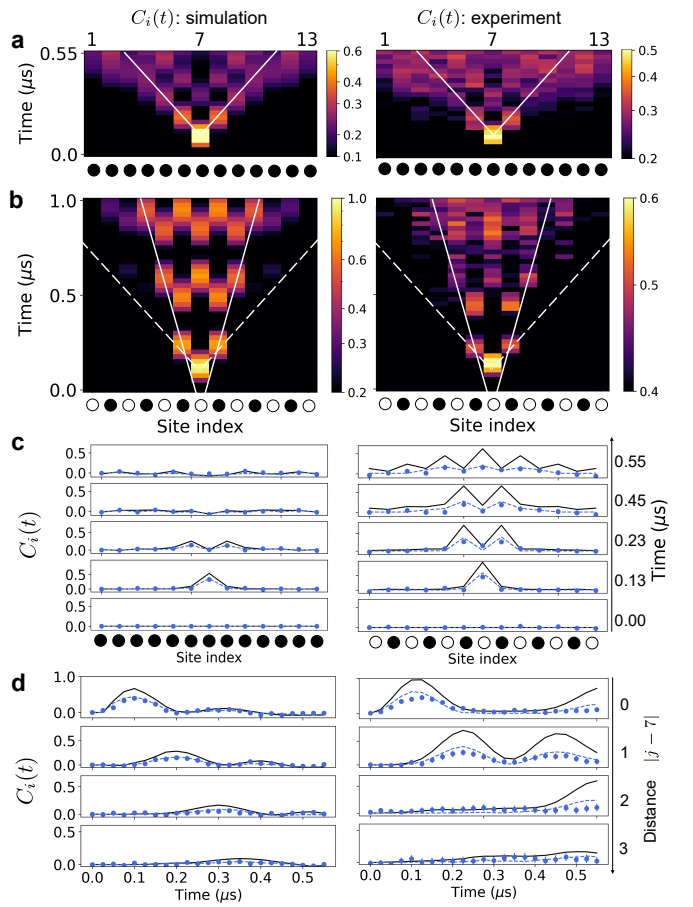


Figure 3 | The observed OTOCs compared to numerical simulations. **a** and **b** for the $|g\rangle$ and $|Z_2\rangle$ initial states, respectively. The left and right panels in **a** and **b** denote respectively experimental and numerical results. A linear lightcone-like operator spreading is observed in both cases. The Z_2 Néel state shows a slower but highly synchronized pattern within the lightcone. Solid (dashed) lines serve as guides to compare with the lightcones of the two different initial states. **c**, Data at peak time of the periodic oscillations to emphasize the persistent and synchronized feature of the OTOC within the lightcone for the Z_2 Néel state. **d**, The spreading of the OTOCs from the addressed central spin (site 7) to other spins, averaged over data for specific spin j ordered by the separation distance $|j - 7|$. Detailed comparisons between experimental (symbols) and two simulated results are plotted in the same sub-figures: one using the experimental ideal model Hamiltonian Eq. (2) (solid lines) and the other considering same Hamiltonian with additional decoherence sources from variations in the atomic positions and single-atom decoherence in the real experiment (dashed lines). We apply background subtraction (as detailed in the SM Sec. IV⁴²) in **c** and **d** to mitigate nonzero bias caused by imperfections in time-reversed evolution.

ing were also found in other ergodicity-breaking systems, such as the logarithmic shaped lightcone in systems with many-body localization⁶⁻⁹, the lightcone with $|Z_2\rangle$ initial state we observe here remains linear at fitted butterfly velocity at about 6 site per microsecond, which is about half of the butterfly velocity for the initial state $|g\rangle$. The characteristic periodic recurrences or “synchronized” oscillations within the lightcone, marking the same time when OTOCs peak across different sites, recur every 0.32 microseconds, which also aligns well with the revival period in the time-forward evolution of the $|Z_2\rangle$ state. Together with the persistent oscillation feature, they indicate that the anomalous spatial-temporal structure is imprinted by the mechanism of quantum many-body scars. Experimental imperfections in the time-reversed evolution reduces the OTOC amplitude in the long-time, as discussed in SM Sec. III⁴², yet longer-lasting periodic revivals remain visible in comparison to typical state under the same experimental con-

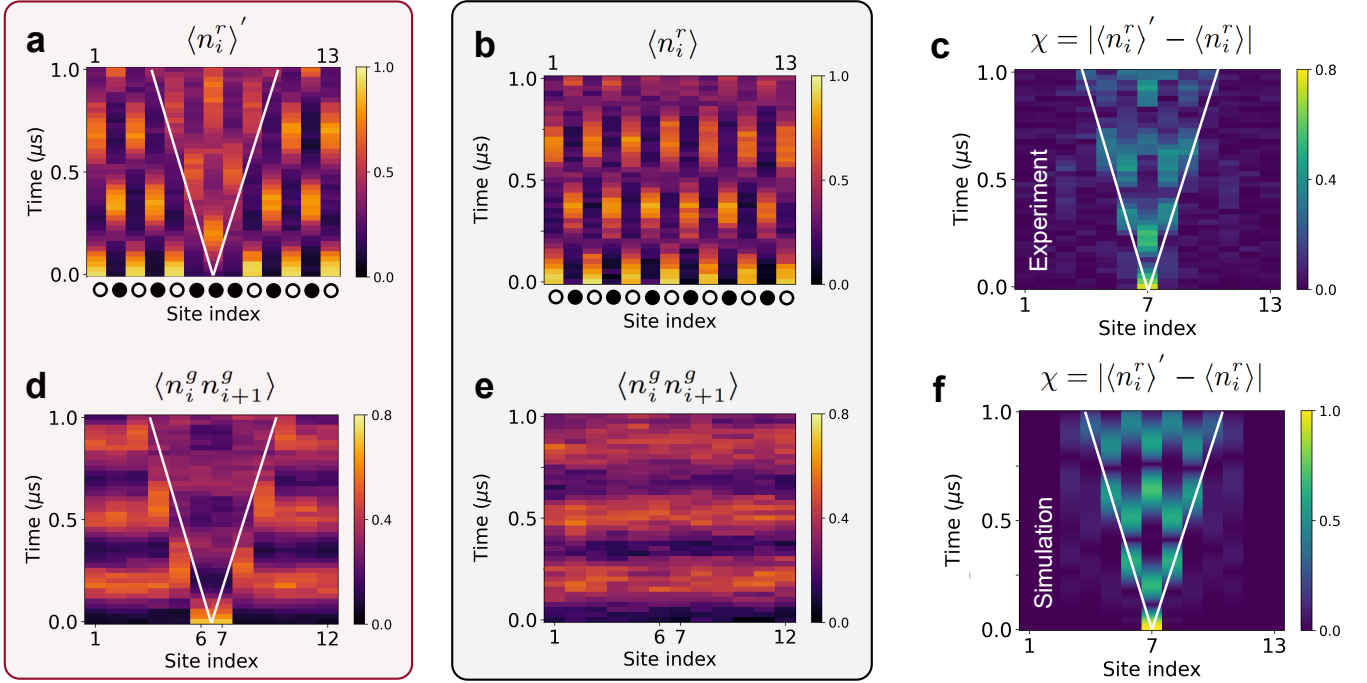


Figure 4 | Rydberg atom density and correlation propagation. Two distinct experiments are performed to investigate the dynamics of information scrambling through local density and correlation propagation, based on dynamics employing initial states $|\mathbf{Z}_2\rangle$ and $|\mathbf{Z}'_2\rangle = \sigma_x^{(7)}|\mathbf{Z}_2\rangle$, differing by a local spin flip to the central Rydberg atom. Panels **a** and **b** present a comparative analysis of the expectation values for the local Rydberg atom density, highlighting the nonlocal differences induced from a local perturbation in the initial state following the dynamical evolution. Panels **c** and **d** further elucidate the local Rydberg atom density differences, experimental data with numerical simulations. The emergence of an analogous honeycomb-like synchronized structure within the lightcone mirrors the characteristic pattern observed for OTOC. Panels **d** and **e** depict the nearest-neighbor correlator of the ground state density, $\langle n_i^g n_{i+1}^g \rangle$, which is interpreted as the anti-ferromagnetic domain wall density, from the same experiments as in **a** and **b**.

ditions.

Local Rydberg atom density and two-body correlation. To affirm the observed slower information spreading and the persistent honeycomb-like structure within the OTOC lightcone, we study the time-forward evolution of the $|\mathbf{Z}_2\rangle$ state and analyze directly its local Rydberg atom density and the propagation of two-body correlation.

Figures 4a and 4b presents the dynamics of the $|\mathbf{Z}'_2\rangle = \sigma_x^{(7)}|\mathbf{Z}_2\rangle$ and $|\mathbf{Z}_2\rangle$ states, respectively. The former is prepared by flipping the Rydberg atom at the central site to its ground state. We find this local disturbance in the initial state disperses into the entire system as well. The data for local Rydberg atom density presented in Fig. 4a reveals a similar persistent oscillation and distinct lightcone boundaries. Both inside and outside of these boundaries, the periodic oscillations exhibit varying rhythms and amplitudes.

From the original data in Figs. 4a and 4b, we obtain Fig. 4c by computing the difference of local Rydberg atom densities between the two experiments with different initial states

$$\chi = |\langle n_i^r \rangle' - \langle n_i^r \rangle|, \quad (4)$$

where $\langle n_i^r \rangle$ and $\langle n_i^r \rangle'$ are the expectation values of local Rydberg atom density operator of the two initial states $|\mathbf{Z}_2\rangle$ and $|\mathbf{Z}'_2\rangle$. They agree well with the numerical results in Fig. 4f and are shown to capture the same essential features of anomalous information scrambling as for OTOCs, including the slower information spreading and the persistent oscillations.

We further explore the transport of two-body correlations^{43,44} as indicators for information scrambling. Figures 4d and 4e show the correlations between nearest neighbors, $\langle n_i^g n_{i+1}^g \rangle$, where $n_i^g = (1 - \sigma_z^{(i)})/2$ is the local ground state atom density at site i . Given the constraint

imposed by Rydberg blockade, where nearest-neighbor atoms cannot simultaneously occupy Rydberg state, one expects $\langle n_i^r n_{i+1}^r \rangle = 0$, and the nearest-neighbor correlator hence reflects ferromagnetic correlation against the background of a Z_2 Néel state: $\langle n_i^g n_{i+1}^g \rangle = \frac{1}{2}(1 + \langle \sigma_z^{(i)} \sigma_z^{(i+1)} \rangle)$. Consequently, this data can be interpreted as the propagation of domain walls, behaving as quasi-particle excitations in the anti-ferromagnetic system. Specifically, two domain walls are initially created at the center by the spin flip operation and subsequently observed to propagate out towards the boundaries. The propagation speed for the lightcone boundaries is found comparable to butterfly velocity observed for the OTOCs and the local Rydberg atom density for the $|\mathbf{Z}_2\rangle$ state. Notably, this speed is also about half of butterfly velocity seen for a typical state, indicating a slower rate of information spreading.

Discussions. Finally, we remark that, due to the time-forward and backward Hamiltonian evolution and interleaved local operators, the persistent oscillations of OTOCs inside the lightcone cannot be directly deduced from the eigenstate decomposition of initial states. As a result, our observed oscillations of OTOCs is distinct from previous reported periodic revivals of local densities³⁶ in essential ways. Indeed, our experimental results provide valuable insights into the intricate dynamics of quantum many-body scars and their pivotal roles in information scrambling process. The unique OTOC signatures of Z_2 Néel states¹⁰, namely the slower butterfly velocity and the persistent oscillations within the lightcone are observed for the first time. The persistent oscillations within the lightcone are in stark contrast to the rapid decay of oscillation amplitude inside the lightcone observed for generic states randomly selected from the Hilbert space in this model as well as in other chaotic systems. Unlike full ergodicity-breaking systems, such

as in many-body localization with a logarithmic lightcone, information spreading of our Rydberg atom array maintains a linear expansion. These signatures are imprinted with quantum many-body scars and further corroborate with measurements of local Rydberg atom density difference and the spreading of two-body correlations.

In this work, the challenge for time-reversed evolution is overcome by taking advantage of the inherent constraint imposed by the strong van der Waals interaction. Such a technique is potentially extendable to the non-resonant regime, where synthetic spin exchange interactions emerge from blockade constraints in second-order perturbation theory⁴⁵. By selectively adjusting the detuning, the interaction sign can likewise be flipped, making it possible to probe different dynamical phase such as quantum walk, localization and dynamical phase transitions with OTOCs in the future. In addition, our demonstrated techniques in measuring OTOCs for the Rydberg atom array platform would prove valuable as well to a variety of other studies including Hilbert space fragmentation^{46,47}, quantum memory⁴⁸, and quantum sensing⁴⁹.

Note that, during the preparation of this manuscript, we became aware of related work by the group of Prof. Lin Li at HUST, which explores similar quantum information scrambling phenomena.

1. Swingle, B. Unscrambling the physics of out-of-time-order correlators. *Nat. Phys.* **14**, 988–990 (2018).
2. Lewis-Swan, R. J., Safavi-Naini, A., Kaufman, A. M. & Rey, A. M. Dynamics of quantum information. *Nat. Rev. Phys.* **1**, 627–634 (2019).
3. Xu, S. & Swingle, B. Scrambling dynamics and out-of-time-ordered correlators in quantum many-body systems. *PRX Quantum* **5**, 010201 (2024).
4. Rigol, M., Dunjko, V. & Olshanii, M. Thermalization and its mechanism for generic isolated quantum systems. *Nature* **452**, 854–858 (2008).
5. Nandkishore, R. & Huse, D. A. Many-body localization and thermalization in quantum statistical mechanics. *Annu. Rev. Condens. Matter Phys.* **6**, 15–38 (2015).
6. Abanin, D. A., Altman, E., Bloch, I. & Serbyn, M. Colloquium: Many-body localization, thermalization, and entanglement. *Rev. Mod. Phys.* **91**, 021001 (2019).
7. Deng, D.-L., Li, X., Pixley, J. H., Wu, Y.-L. & Das Sarma, S. Logarithmic entanglement lightcone in many-body localized systems. *Phys. Rev. B* **95**, 024202 (2017).
8. Fan, R., Zhang, P., Shen, H. & Zhai, H. Out-of-time-order correlation for many-body localization. *Sci. Bull.* **62**, 707–711 (2017).
9. Huang, Y., Zhang, Y.-L. & Chen, X. Out-of-time-ordered correlators in many-body localized systems. *Ann. Phys. (Berlin)* **529**, 1600318 (2017).
10. Yuan, D., Zhang, S.-Y., Wang, Y., Duan, L.-M. & Deng, D.-L. Quantum information scrambling in quantum many-body scarred systems. *Phys. Rev. Res.* **4**, 023095 (2022).
11. Li, J. *et al.* Measuring out-of-time-order correlators on a nuclear magnetic resonance quantum simulator. *Phys. Rev. X* **7**, 031011 (2017).
12. Wei, K. X., Ramanathan, C. & Cappellaro, P. Exploring localization in nuclear spin chains. *Phys. Rev. Lett.* **120**, 070501 (2018).
13. Niknam, M., Santos, L. F. & Cory, D. G. Sensitivity of quantum information to environment perturbations measured with a nonlocal out-of-time-order correlation function. *Phys. Rev. Res.* **2**, 013200 (2020).
14. Gärtner, M. *et al.* Measuring out-of-time-order correlations and multiple quantum spectra in a trapped-ion quantum magnet. *Nat. Phys.* **13**, 781–786 (2017).
15. Landsman, K. A. *et al.* Verified quantum information scrambling. *Nature* **567**, 61–65 (2019).
16. Joshi, M. K. *et al.* Quantum information scrambling in a trapped-ion quantum simulator with tunable range interactions. *Phys. Rev. Lett.* **124**, 240505 (2020).
17. Green, A. M. *et al.* Experimental measurement of out-of-time-ordered correlators at finite temperature. *Phys. Rev. Lett.* **128**, 140601 (2022).
18. Mi, X. *et al.* Information scrambling in quantum circuits. *Science* **374**, 1479–1483 (2021).
19. Braumüller, J. *et al.* Probing quantum information propagation with out-of-time-ordered correlators. *Nat. Phys.* **18**, 172–178 (2022).
20. Zhao, S. K. *et al.* Probing operator spreading via floquet engineering in a superconducting circuit. *Phys. Rev. Lett.* **129**, 160602 (2022).
21. Wang, J.-H. *et al.* Information scrambling dynamics in a fully controllable quantum simulator. *Phys. Rev. Res.* **4**, 043141 (2022).
22. Chen, B. *et al.* Detecting the out-of-time-order correlations of dynamical quantum phase transitions in a solid-state quantum simulator. *Appl. Phys. Lett.* **116** (2020).
23. Nie, X. *et al.* Experimental observation of equilibrium and dynamical quantum phase transitions via out-of-time-ordered correlators. *Phys. Rev. Lett.* **124**, 250601 (2020).
24. Nie, X. *et al.* Detecting scrambling via statistical correlations between randomized measurements on an nmr quantum simulator. *arxiv:1903.12237* (2019).
25. Vermersch, B., Elben, A., Sieberer, L. M., Yao, N. Y. & Zoller, P. Probing scrambling using statistical correlations between randomized measurements. *Phys. Rev. X* **9** (2019).
26. Saffman, M., Walker, T. G. & Mølmer, K. Quantum information with rydberg atoms. *Rev. Mod. Phys.* **82**, 2313–2363 (2010).
27. Browaeys, A. & Lahaye, T. Many-body physics with individually controlled rydberg atoms. *Nat. Phys.* **16**, 132–142 (2020).
28. Wu, X. *et al.* A concise review of rydberg atom based quantum computation and quantum simulation*. *Chinese Physics B* **30**, 020305 (2021).
29. Morgado, M. & Whitlock, S. Quantum simulation and computing with rydberg-interacting qubits. *AVS Quantum Sci.* **3** (2021).
30. Manetsch, H. J. *et al.* A tweezer array with 6100 highly coherent atomic qubits. *arxiv:2403.12021* (2024).
31. Ma, S. *et al.* Gate operations on nuclear spin qubits in an optical tweezer array of ¹⁷¹Yb atoms. *Phys. Rev. X* **12**, 021028 (2022).
32. Anand, S. *et al.* A dual-species rydberg array. *Nat. Phys.* (2024).
33. Bernien, H. *et al.* Probing many-body dynamics on a 51-atom quantum simulator. *Nature* **551**, 579 (2017).
34. Semeghini, G. *et al.* Probing topological spin liquids on a programmable quantum simulator. *Science* **374**, 1242–1247 (2021).
35. Kim, K., Yang, F., Mølmer, K. & Ahn, J. Realization of an extremely anisotropic heisenberg magnet in rydberg atom arrays. *Phys. Rev. X* **14**, 011025 (2024).
36. Bluvstein, D. *et al.* Controlling quantum many-body dynamics in driven rydberg atom arrays. *Science* **371**, 1355–1359 (2021).
37. Turner, C. J., Michailidis, A. A., Abanin, D. A., Serbyn, M. & Papić, Z. Weak ergodicity breaking from quantum many-body scars. *Nat. Phys.* **14**, 745–749 (2018).
38. Serbyn, M., Abanin, D. A. & Papić, Z. Quantum many-body scars and weak breaking of ergodicity. *Nat. Phys.* **17**, 675–685 (2021).
39. Bies, W. E., Kaplan, L. & Heller, E. J. Scarring effects on tunneling in chaotic double-well potentials. *Phys. Rev. E* **64**, 016204 (2001).
40. Deutsch, J. M. Quantum statistical mechanics in a closed system. *Phys. Rev. A* **43**, 2046–2049 (1991).
41. Srednicki, M. Chaos and quantum thermalization. *Phys. Rev. E* **50**, 888–901 (1994).
42. Supplementary material.
43. Jurcevic, P. *et al.* Quasiparticle engineering and entanglement propagation in a quantum many-body system. *Nature* **511**, 202–205 (2014).
44. Richerme, P. *et al.* Non-local propagation of correlations in quantum systems with long-range interactions. *Nature* **511**, 198–201 (2014).
45. Yang, F., Yang, S. & You, L. Quantum transport of rydberg excitons with synthetic spin-exchange interactions. *Phys. Rev. Lett.* **123** (2019).
46. Moudgalya, S., Bernevig, B. A. & Regnault, N. Quantum many-body scars and hilbert space fragmentation: a review of exact results. *Rep. Prog. Phys.* **85**, 086501 (2022).
47. Buča, B. Out-of-time-ordered crystals and fragmentation. *Phys. Rev. Lett.* **128**, 100601 (2022).
48. Lvovsky, A. I., Sanders, B. C. & Tittel, W. Optical quantum memory. *Nat. Photon.* **3**, 706–714 (2009).
49. Dooley, S. Robust quantum sensing in strongly interacting systems with many-body scars. *PRX Quantum* **2**, 020330 (2021).

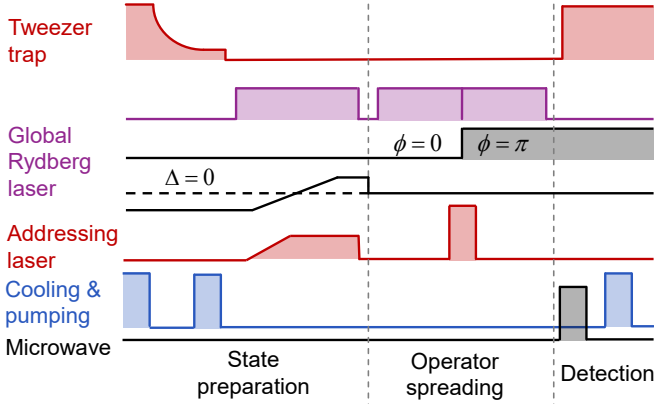
Acknowledgments. We acknowledge significant help and enlightening discussions with Dong-Ling Deng and Dong Yuan. We acknowledge helpful contributions by Xiaoling Wu, Songtao Huang, Yuanjiang Tang, Chenyuan Li and Xiangliang Li in the early stages of building up the experimental platform. XL also acknowledges constructive discussions with Fan Yang and Guoxian Su. This work is supported by the Innovation Program for Quantum Science and Technology (2021ZD0302100). LY is also supported by NSFC (Grants No. 12361131576 and No. 92265205). MKT is supported by NFSC (Grants. No.12234012 and W2431002).

Author contributions. XL, ZY, YXC and ZXH built the experimental platform under supervision of MKT; XL and LY conceived this study. XL, ZY, YXC, and ZXH performed the experiment and analyzed the data. XL, MKT, and LY wrote the paper.

Competing interests The authors declare no competing interests.

Methods

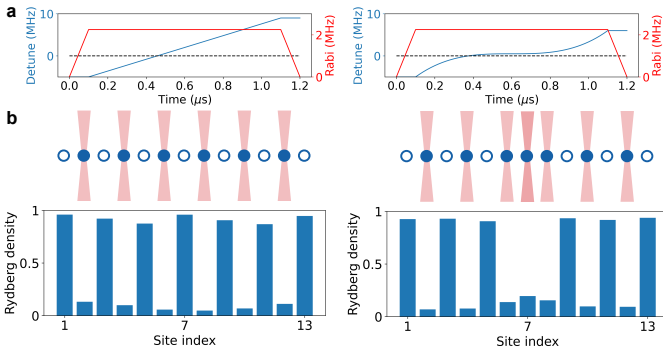
Experimental time sequence



Extended Data Fig. 1 | Time sequence of the experiment.

The experimental time sequence for measuring OTOC is composed of three main steps as in generic Loschmidt echo or interferometry: preparation of the initial state, analog-digital hybrid evolution to spread the encoded operator, and single-atom resolved final state detection (Extended Data Fig. 1).

To prepare the initial state, all atoms are laser cooled and optically pumped into the desired ground state. To prepare the Z_2 antiferromagnetic Néel state, the two-photon detuning of the 420-nm and 1013-nm lasers is adiabatically swept from large negative to large positive values. Better preparation fidelity is achieved by introducing addressing lasers to pin down the selected atoms, forcing them to stay in the ground state. The addressing strategy, adiabatic laser frequency sweep, and experimental results of state preparation are presented in Extended Data Fig. 2.



Extended Data Fig. 2 | Initial state preparation. The $|Z_2\rangle$ state and $|Z_2'\rangle = \sigma_x^{(7)}|Z_2\rangle$ state with one fewer Rydberg atom at the central site. **a**, The $|Z_2\rangle$ state is prepared by adiabatic sweeping of laser parameters. **b**, The $|Z_2'\rangle$ state is prepared as in (a) but the addressing laser pins the central spin to the ground state throughout the adiabatic ramp.

The global Rydberg laser is turned on during the time-forward evolution, while the time-reversed evolution is realized by a sudden π phase jump to the Rydberg coupling laser, which introduces a negative sign to the effective PXP Hamiltonian. The phase jump is directly programmed into the arbitrary waveform generator, which controls the phase of the 420-nm laser through a single-pass acousto-optic modulator. A brief dip of around 10 ns appears in the laser power due to

the drop in diffraction efficiency of the AOM during the sudden phase shift. Nevertheless, this time duration is so short that the undesired effect can be neglected over the intended evolution time. Phase imprinting is achieved using the same addressing lasers for preparation of the Z_2 initial state.

Single-atom resolved state detection is carried out by switching on the trapping tweezers. Ground state atoms are recaptured, while Rydberg atoms are lost. The recaptured atom is detected by fluorescence imaging. We use a strong microwave pulse to ionize the Rydberg states in a short time before recapture to enhance detection efficiency.

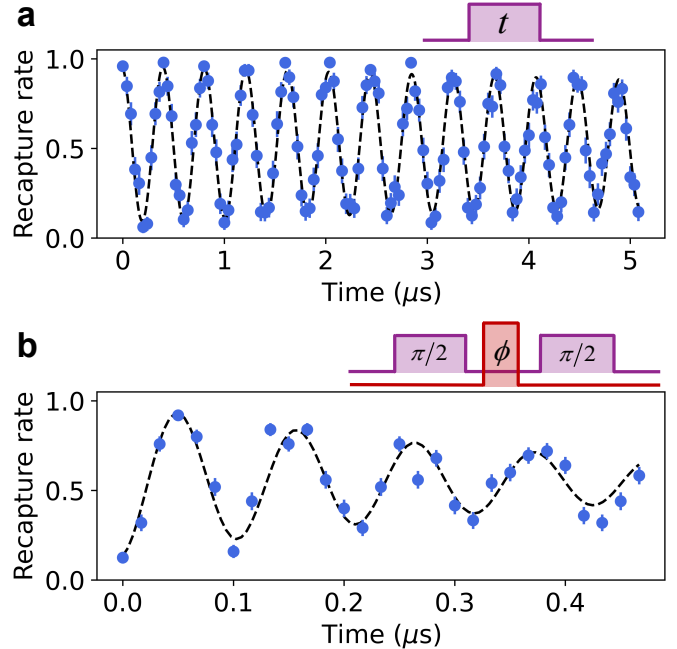
Calibration of single qubit Rabi oscillation and phase imprinting

The single-qubit Rabi oscillation is driven by counter-propagating global lasers with two-photon Rabi frequency of 2 to 2.5 MHz (Extended Data Fig. 3a).

The single-qubit Z operation is realized via an AC Stark shift induced by an addressing laser. This laser is previously used to remove and rearrange the randomly loaded atom array into a defect-free array as well as to facilitate the preparation of the select initial state.

The amount of phase imprinted is calibrated with a single-atom Ramsey experiment (Extended Data Fig. 3b). Phase accumulation is probed with two $\pi/2$ pulses. The oscillation period is approximately $0.11 \mu\text{s}$, implying that a $0.055 \mu\text{s}$ Z gate operation corresponding to a π pulse.

The coherence of the addressing phase is significantly reduced compared to the global one due to the fluctuating atomic positions relative to the narrow waist of the addressing laser. Enhanced coherence can be achieved by improved cooling and by expanding the waist of the addressing laser during phase imprinting with a focal length tunable lens.



Extended Data Fig. 3 | Calibrations for single qubit operation. **a**, Global Rabi oscillation. **b**, Addressing phase imprinting.

Supplementary information: Observation of anomalous information scrambling in a Rydberg atom array

Xinhui Liang,^{1,2,*} Zongpei Yue,^{1,3,*} Yu-Xin Chao,^{1,3} Zhen-Xing
Hua,^{1,3} Yige Lin,⁴ Meng Khoon Tey,^{1,3,5,†} and Li You^{1,2,3,5,‡}

¹*State Key Laboratory of Low Dimensional Quantum Physics,*

Department of Physics, Tsinghua University, Beijing 100084, China

²*Beijing Academy of Quantum Information Sciences, Beijing 100193, China*

³*Frontier Science Center for Quantum Information, Beijing 100084, China*

⁴*Division of Time and Frequency Metrology,*

National Institute of Metrology, Beijing 100029, People's Republic of China

⁵*Hefei National Laboratory, Hefei, Anhui 230088, China*

(Dated: October 22, 2024)

CONTENTS

I. Introduction to OTOC	2
II. OTOC for special initial states	4
III. Imperfections in time-reversed evolution	5
IV. Error compensation and subtraction	7
References	9

I. INTRODUCTION TO OTOC

Quantum information scrambling is customarily measured by the four-point correlator with an unusual time ordering, defined as

$$F(t) = \langle \psi | W^\dagger(t) V^\dagger W(t) V | \psi \rangle, \quad (1)$$

where $W(t) = e^{i\mathcal{H}t} W e^{-i\mathcal{H}t}$ represents the operator's evolution in the Heisenberg picture. This expression measures the overlap between the two states $W(t)V|\psi\rangle$ and $VW(t)|\psi\rangle$, which share the same initial state but differ in the sequence of operations applied. For unitary operators, the above OTOC connects to the squared commutator

$$C(t) = \langle \psi | [W(t), V]^\dagger [W(t), V] | \psi \rangle, \quad (2)$$

through the relation $C(t) = 2\{1 - \text{Re}[F(t)]\}$, emphasizing the development of noncommutativity between two quantum operations over time.

The spatial propagation of local quantum operators can be monitored by selecting W and V as local operators, exemplified by Pauli matrices $\sigma_\mu^{(i)}$, ($\mu = x, y, z$) of the i -th qubit. The commutator $[\sigma_\mu^{(i)}(t), \sigma_\nu^{(j)}]$ in the space-time diagram illustrates how information transports from one local site to another. In system with local interaction, the emergence of a lightcone with a finite velocity affirms the so-called Lieb-Robinson bounds for information propagation.

* These authors contributed equally to this work.

† mengkhooon`tey@mail.tsinghua.edu.cn

‡ lyou@mail.tsinghua.edu.cn

More generally, the spreading of local information does not always adhere to a ballistic pattern but can exhibit diverse growth behaviors, thereby be employed to characterize different quantum dynamical phases[1]. As the long-range connectivity of a system increases, the shape of the information lightcone transforms from ballistic to exponential form. The corresponding OTOC exhibits rapidly decaying oscillation amplitude inside the lightcone and converges to a steady value, as a signature of many-body quantum chaos. Conversely, increasing disorder in a system leads to a slowdown in information propagation, resulting in a logarithmic shaped lightcone in a many-body localization system. However, the structure inside the light-core is rarely studied and it was predicted theoretically that persistent oscillations can occur with Z_2 Néel state[2].

OTOC in general can not be directly observed in an analog quantum simulator. Under some conditions, however, for instance when the initial state is an eigenstate of the operator V (with eigenvalue v_i), the expression for the OTOC in Eq. (1) simplifies into

$$F_{ij}(t) = v_j \langle \Psi_i(t) | V_j^\dagger | \Psi_i(t) \rangle, \quad (3)$$

where $|\Psi_i(t)\rangle = e^{-i\mathcal{H}_-t} W_i e^{-i\mathcal{H}_+t} |\psi\rangle$, with H_+ the time forward evolution Hamiltonian, and $H_- = -H_+$ for the time-reversed evolution. This opens up the possible measurement of OTOC experimentally through the properties of final state in Loschmidt echo experiment.

In the OTOC measurement as we report, a fast implementation for a single $\sigma_x^{(i)}$ operator is also challenging due to the inevitable $\sigma_z^{(i)}$ operation introduced by the a.c.-Stark shift from the two-photon coupling through a finite intermediate state detuning. On the other hand, a fast single-qubit rotation operator can be effectively induced with the a.c.-Stark shift from the site addressed laser. With default measurement carried out in the Z base, we thus focus on the ZZ-OTOC ($W = \sigma_z^{(i)}, V = \sigma_z^{(j)}$), the corresponding OTOC then takes the following simple form

$$F_{ij}^{ZZ}(t) = (-1)^{\langle n_j^r(0) \rangle + 1} [2 \langle n_j^r(t) \rangle_i - 1], \quad (4a)$$

$$C_{ij}^{ZZ}(t) = |\langle n_j^r(t) \rangle_i - \langle n_j^r(0) \rangle|, \quad (4b)$$

where $\langle n_j^r(0) \rangle = \langle \psi_0 | n_j^r | \psi_0 \rangle$ and $\langle n_j^r(t) \rangle_i = \langle \Psi_i(t) | n_j^r | \Psi_i(t) \rangle$ are the Rydberg densities of the initial states and the evolved states after echo time t following phase imprinting operation at site i respectively.

II. OTOC FOR SPECIAL INITIAL STATES

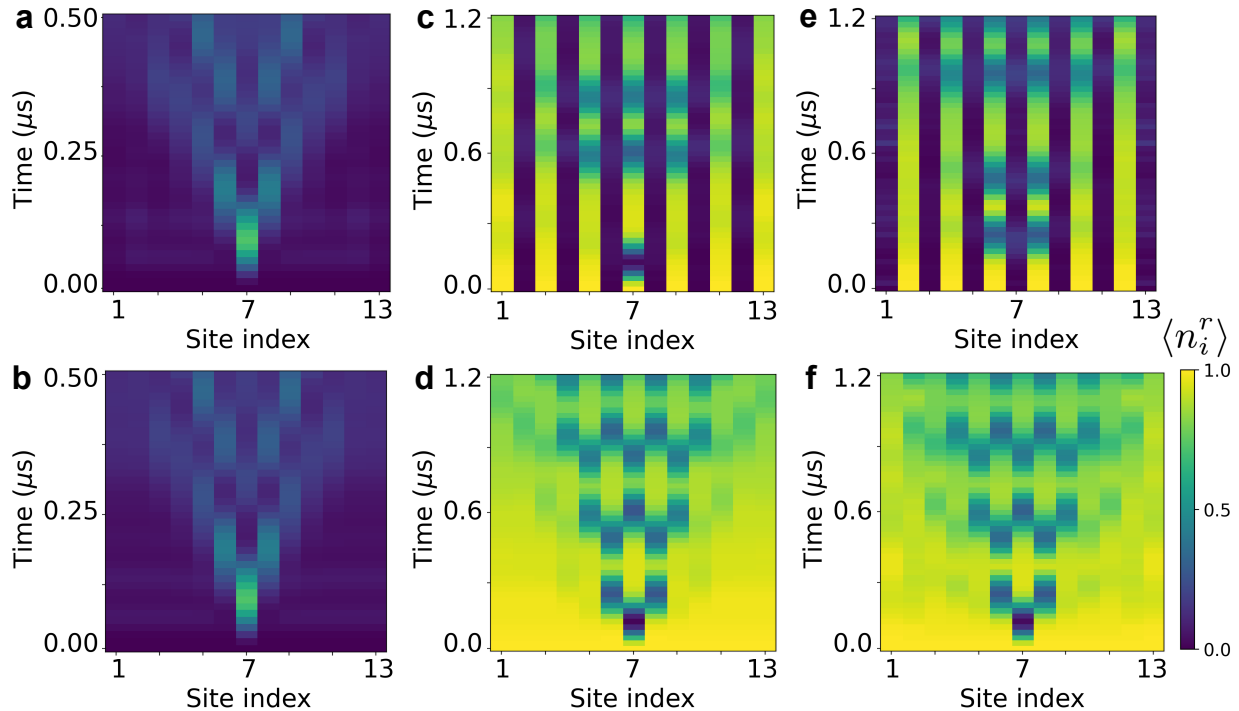


FIG. 1. Comparisons of the different OTOCs to be measured in our experiment. These results of the Rydberg density (according to the color bar) come from numerical simulated evolution of Rydberg Hamiltonian (Eq. 5) for a 13-atom chain over time with different initial states. Panels **a** and **b** depict results from initial states $|\mathbf{g}\rangle = |gg\dots g\rangle$, while panels **c** through **f** show results from \mathbf{Z}_2 Néel states. In **a** and **c**, the measurement site index i is changed, while in **b** and **d**, the addressing site index j is altered. Panel **e** mirrors the procedure of **c** but employs the complementary $\bar{\mathbf{Z}}_2$ state $|grgr\dots grg\rangle$ in place of the state $|rgrg\dots rgr\rangle$ in **c**. Panel **f** combines information from **c** and **e**. Based on these results, it becomes evident that panels **a** and **b**, as well as **d** and **f**, exhibit similar structures in information scrambling. Minor discrepancies in numerical values are attributed to finite size effects and are negligible during the early stages of evolution, before information spreading reaches the open boundaries.

Specifically for the ZZ-OTOC, we consider the non-commutativity of the operators F_{ij} . There are two main approaches to visualize information spreading with OTOC: the depen-

dence on the operator index j or on the site index i . Notably, for the state $|\mathbf{g}\rangle = |gg\dots g\rangle$, the two OTOCs are found to exhibit similar structures. In our experiment, we choose to vary the site index i to leverage on the highly paralleled measurements in the Rydberg atom array simulator.

For Néel states, the OTOC measurement needs to be slightly modified. We find that varying the operator index j provides better contrast for OTOC, as discussed before [2]. To fully utilize the parallel measurement capabilities, we prepare two complementary Néel states $|\mathbf{Z}_2\rangle$ and $|\bar{\mathbf{Z}}_2\rangle$ to obtain the OTOC for odd- and even-numbered sites, respectively. These measurements are then combined to form a structure giving an analogous structure similar to that of varying the operator index j as shown in Fig. 1.

III. IMPERFECTIONS IN TIME-REVERSED EVOLUTION

We will now discuss simulation results based on the model Rydberg Hamiltonian assuming perfect controls and including only the nearest-neighbor (NN) interactions. The primary errors due to imperfections are caused by the deviations of the physical Hamiltonian from the ideal PXP model, particularly with respect to the neglect of next-nearest-neighbor (NNN) interactions, followed by second-order virtual coupling to states that violate the blockade condition. The decrease in contrast in Z_2 Néel state can also come from additional initial state preparation infidelities.

The choice of interatomic spacing in the Rydberg array simulator can be leveraged to balance and minimize errors in OTOC measurements. By carefully selecting a suitable spacing, one can optimize the trade-off between NNN interactions and other errors, thereby enhancing the accuracy and reliability of the experimental results.

The experimental results for single atom OTOC are presented in Fig. 2. The signal is found to be primarily concentrated on the addressed atom located at the center of the Rydberg array, exhibiting behavior equivalent to a t - π - t single atom Rabi oscillation. Imperfections in the time-reversed evolution of other atoms are observed as well, and are found to primarily come from NNN and longer-range interactions.

To quantitatively assess the impact of imperfections in the time-reversed evolution on the

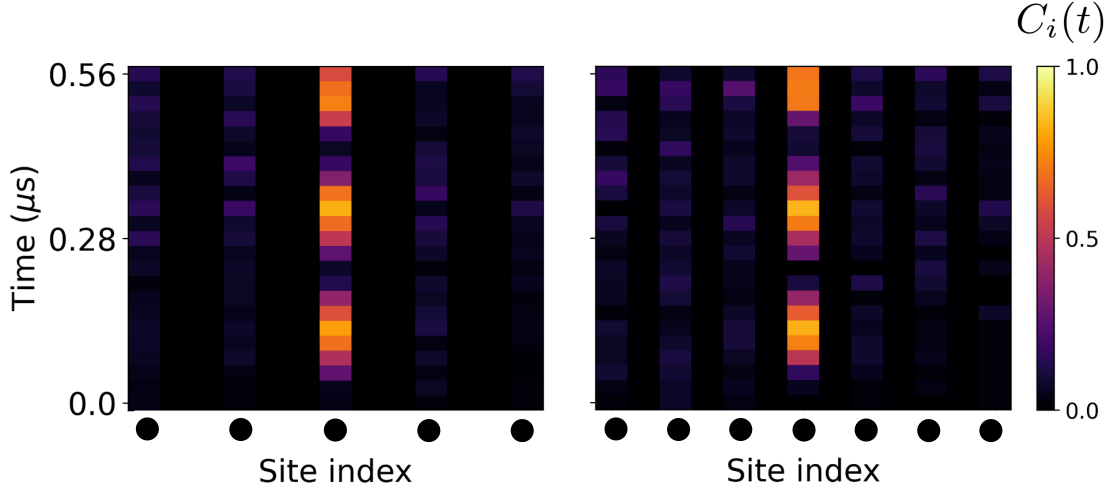


FIG. 2. OTOC of non-interacting atom chain. Compared to the OTOC of 13 atoms with the initial state $|\mathbf{g}\rangle = |gg\dots g\rangle$ in the main text, the atoms are rearranged to a larger inter-atomic spacing, effectively eliminating NN interactions. The information concentrate on the addressing atoms and can not spread to other site without inter-atom interactions.

OTOC, we performed numerical simulations of the Rydberg Hamiltonian

$$H = \frac{\Omega}{2} \sum_i \sigma_x^{(i)} - \Delta \sum_i n_i^r + \sum_{i<j} V(\mathbf{r}_{ij}) n_i^r n_j^r, \quad (5)$$

under various approximations to the system parameters. Our simulations reveal that, when the NN interaction strength is sufficiently large at 120 MHz and interactions beyond NN are neglected, the system closely mimics the behavior of the PXP Hamiltonian

$$H = \frac{\Omega}{2} \sum_{i=1}^{L-1} P_{i-1} \sigma_x^{(i)} P_{i+1}. \quad (6)$$

In this case, the time-reversed evolution is nearly perfect, resulting in a clear and distinct OTOC signal that easily stands out from the background noise. However, when the blockade condition is relaxed to the NN interaction strength of 12 MHz, we observe a periodic rise in the background noise due to leakage into otherwise forbidden subspaces. Furthermore, the inclusion of NNN interaction, which is 64 times weaker than the NN interaction, introduces even more significant errors. Given the fixed ratio between NN and NNN interaction strengths, choosing a NN interaction of 12 MHz represents a compromise between these two error sources. Additionally, experimental imperfections, such as variations in atom positions lead to decoherence of Ramsey signals, as well as fluctuations in interactions, single-spin de-

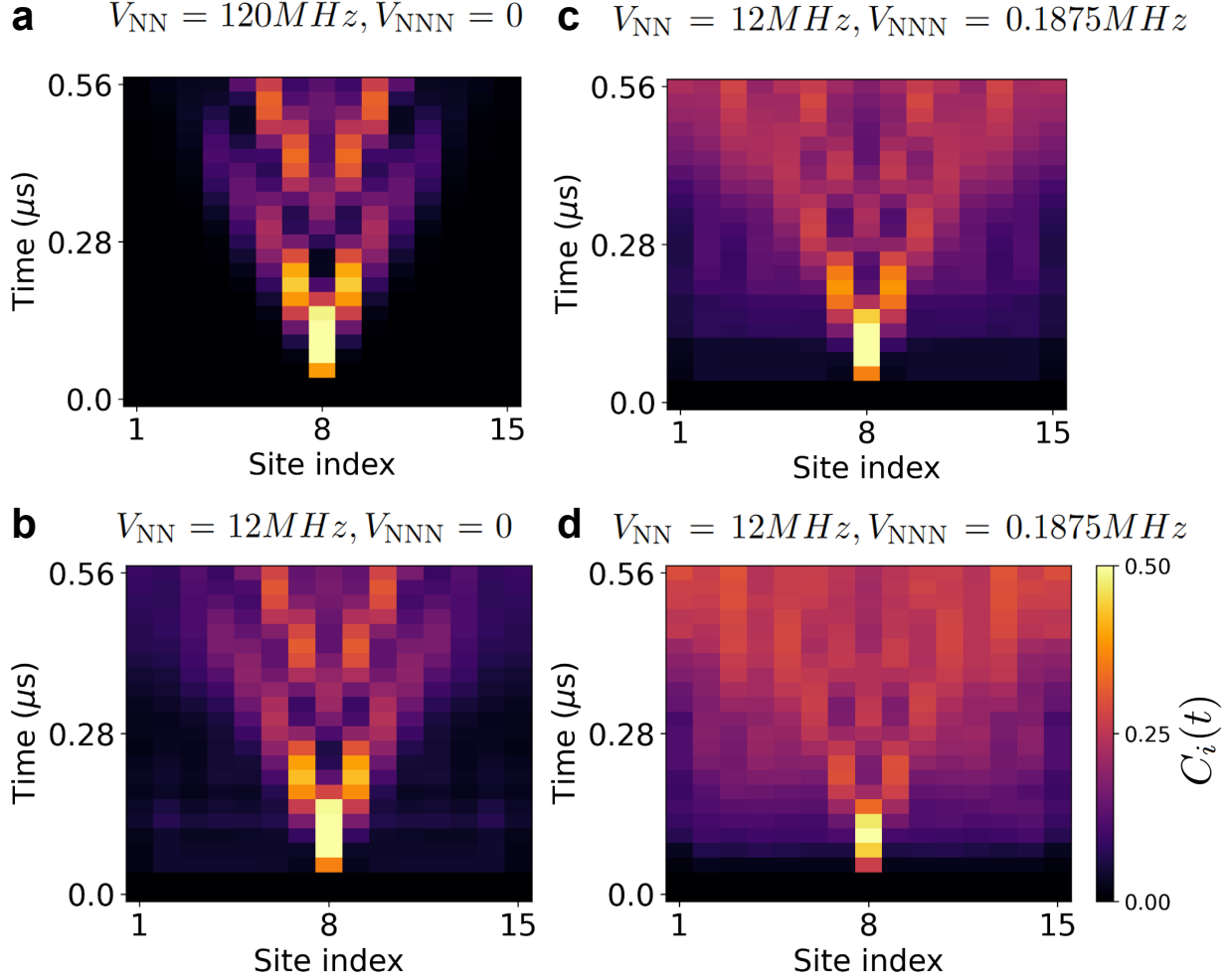


FIG. 3. Numerical results for Rydberg density or $C_i(t)$ for the initial state $|g\rangle = |gg\dots g\rangle$ at different parameters $\Delta = 0, \Omega_i = 2.5 MHz$ **a**, $V_{NN} = 120 MHz, V_{NNN} = 0$, **b**, $V_{NN} = 12 MHz, V_{NNN} = 0$, **c**, $V_{NN} = 12 MHz, V_{NNN} = 0.1875 MHz$, **d**, for the same parameters as in **c** but with noise channels including variations in atom positions, single-spin dephasing and depolarization.

phasing, and depolarization, all of the above contribute to deteriorating signal-to-noise ratio for the long-time OTOC. Consequently, the contrast of the OTOC becomes less pronounced during extended time evolution.

IV. ERROR COMPENSATION AND SUBTRACTION

In our experiments, an extra detuning is introduced to partially null out the NNN interactions in the time-reversed evolution as first suggested in the Ref. [2]. It remains

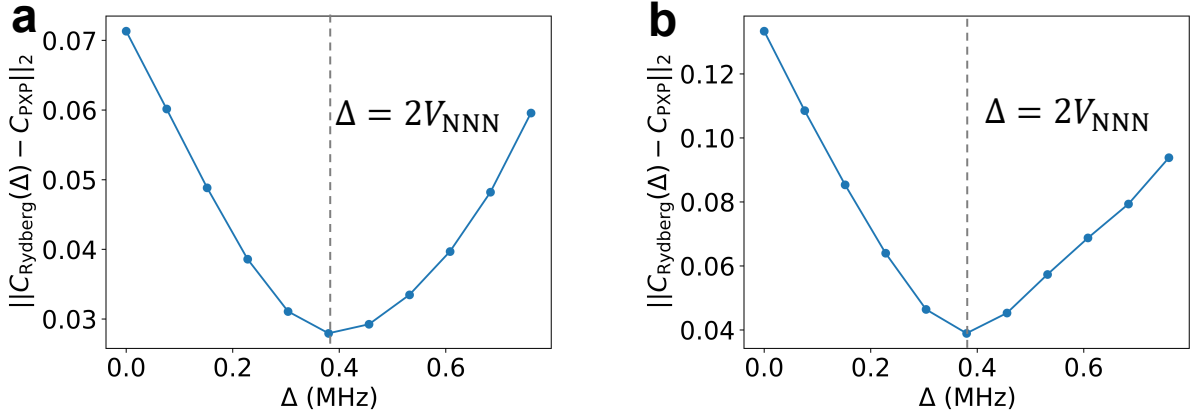


FIG. 4. Error compensation. Optimize the compensation detuning to minimize the distance $\|C_{\text{Rydberg}}(\Delta) - C_{\text{PXP}}\|_2$ between the OTOC with real Rydberg array Hamiltonian and with ideal PXP Hamiltonian. The optimal detuning is approximately twice the NNN interaction strength, for both (a) $|g\rangle = |gg\dots g\rangle$ and (b) $|Z_2\rangle = |rgrg\dots rgr\rangle$ studied in the main text.

constant throughout the time-forward and time-reversed evolution and is optimized based on comparisons with numerical results for the ideal PXP model (see Fig. 4). Notably, for the $|g\rangle$ and both $|Z_2\rangle$ states, optimal compensation favors a detuning value that is approximately twice the strength of the NNN interaction.

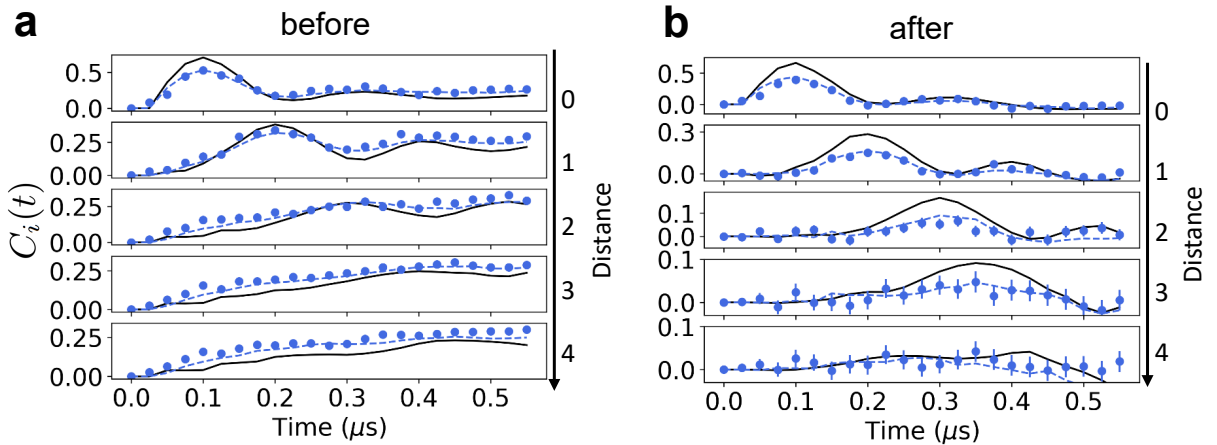


FIG. 5. Results from numerical (solid lines) and experiment (dots) (a) before and (b) after error subtraction.

To mitigate other biased errors in the OTOC, the errors stemming from imperfect time-reversed evolution are subtracted. The subtracted background can be quantified through an

analogous experiment, but without the single-spin Z operator. In our experiments, atoms situated far away from the central one undergo identical global and time-reversed evolution yet remain unaffected by operator spreading during the evolved time, thus they can be employed as a reference for the background (as in common mode rejection). Compared to repeating the experiment for the sole purpose of obtaining the background error, this approach of reference to distant atoms further facilitates the elimination of common-mode noise stemming from long-term shifts in experimental parameters. Fig. 5 shows the results before and after the discussed error subtraction.

-
- [1] S. Xu and B. Swingle, *PRX Quantum* **5**, 010201 (2024).
[2] D. Yuan, S.-Y. Zhang, Y. Wang, L.-M. Duan, and D.-L. Deng, *Phys. Rev. Research* **4**, 023095 (2022).